ACS Energy LETTERS

Open Access

http://pubs.acs.org/journal/aelccp

Letter

Understanding the Role of Triple Phase Boundaries on Coating-Free Solid-State Cathodes

Longlong Wang,[#] Bingkun Hu,[#] Christopher Doerrer,[#] Shengming Zhang, Lechen Yang, Liquan Pi, Max Jenkins, Boyang Liu, Shengda D. Pu, Yi Yuan, Hui Gao, Alex W. Robertson, Patrick S. Grant, Xiangwen Gao,* and Peter G. Bruce*

Cite This: *ACS Energy Lett.* 2026, 11, 1623−1630

Read Online

ACCESS | Metrics & More | Article Recommendations | Supporting Information

ABSTRACT: Sulfide solid electrolytes have high ionic conductivities necessary to achieve high-rate solid-state cathodes at room temperature and low pressure. Cathode active materials generally require coatings to avoid deleterious oxidative decomposition reactions with the electrolyte. Coatings add cost and complexity to the manufacture. Here we decouple the effect of double and triple phase boundaries on the decomposition in the thick (i.e., ∼110 μm) uncoated solid state cathode. We show that more severe oxidative decomposition of solid electrolytes occurs when the cathode active materials, carbon, and the solid electrolyte coexist, highlighting the importance of the triple phase boundary concerning the decomposition. By regulating the electronic pathways at the triple phase boundary, a thick uncoated electrode at 1 mA cm^{-2} and 2 MPa stack pressure, delivers an initial areal capacity of ∼4.6 mAh cm^{-2} at 30 °C and ∼85% capacity retention after 500 cycles.

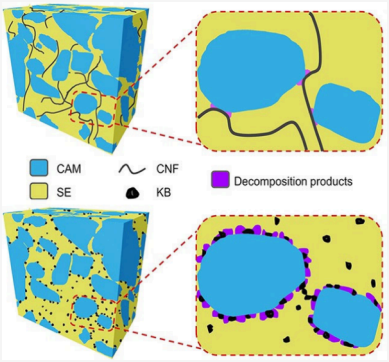

All-solid-state batteries (ASSBs) are viewed as a promising next-generation energy storage technology because of their inherent safety and potentially higher energy/power density compared with conventional liquid Li-ion batteries (LIBs).[1−3] If ASSBs based on ceramic electrolytes are to deliver the high energy densities promised by such batteries, they must employ a high energy density anode, e.g., lithium metal, and a high energy density solid-state cathode (SSC) composed of the cathode active material (CAM) and a solid electrolyte (SE), as well as carbon to facilitate electronic transport through the SSC.[4−6] Moreover, from the practical engineering point of view, the desired stack pressure should be ideally <2 MPa.[1,4,7−10]

Although sulfide-based solid electrolytes (SSEs) have the conductivities necessary to deliver high energy densities at practical rates (mA cm^{-2}) and stack pressures less than a few MPa,[8,11−13] they are readily oxidized at the potentials of nickel-rich CAMs, resulting generally in significant capacity loss on cycling.[14−19] As a result, the CAM particles have to be coated with e.g. $LiNbO_3$, Li_2ZrO_3 or $LiZr_2(PO_4)_3$ to mitigate the reactivity.[8,12,20−24] However, coatings add complexity and cost to the manufacture of batteries and can add a kinetic barrier to operation of the cell.[25−27] It is desirable to avoid coatings if possible.[25,28] Previous reports of uncoated CAM-based ASSBs have indicated that employing a low specific surface area carbon in the SSC could improve performance compared with using a large specific surface area carbon.[16,29−35] The present study provides a mechanistic understanding, including the differences between decomposition products at the triple and double phase boundaries and its relationship to good performance under practical conditions.

Here we investigate the effect of double and triple phase boundaries on the SSE decomposition in the practical thick (i.e., ∼110 μm) SSC with a high CAM ratio (i.e., 75%) at practical cycling conditions (i.e., 1 mA cm^{-2} cycling rate and 2 MPa stack pressure). The SSCs comprise uncoated nickel-rich $LiNi_{0.83}Mn_{0.06}Co_{0.11}O_2$ (NMC), Li_6PS_5Cl, and either carbon nanofibers (CNFs) or Ketjen black (KB). We show that more severe oxidative decomposition of SSEs occurs when the CAM, carbon, and the SSE coexist compared with when only two phases (CAM/SSE or carbon/SSE) are present under practical conditions, highlighting the importance of the triple phase boundary. By regulating the electronic pathways at the triple phase boundary, a ∼110 μm thick uncoated electrode with CNFs at 1 mA cm^{-2} and 2 MPa stack pressure, delivers an areal capacity of ∼4.6 mAh cm^{-2} (182 mAh g^{-1} CAM utilization) at 30 °C on the first cycle (2.5 to 4.3 V) and ∼85% capacity retention after 500 cycles with a 0.03% capacity loss per cycle. Our findings provide new insights into the design of high-performance practical SSCs for ASSBs.

Received: August 14, 2025
Revised: January 6, 2026
Accepted: January 27, 2026
Published: January 30, 2026

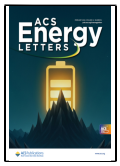

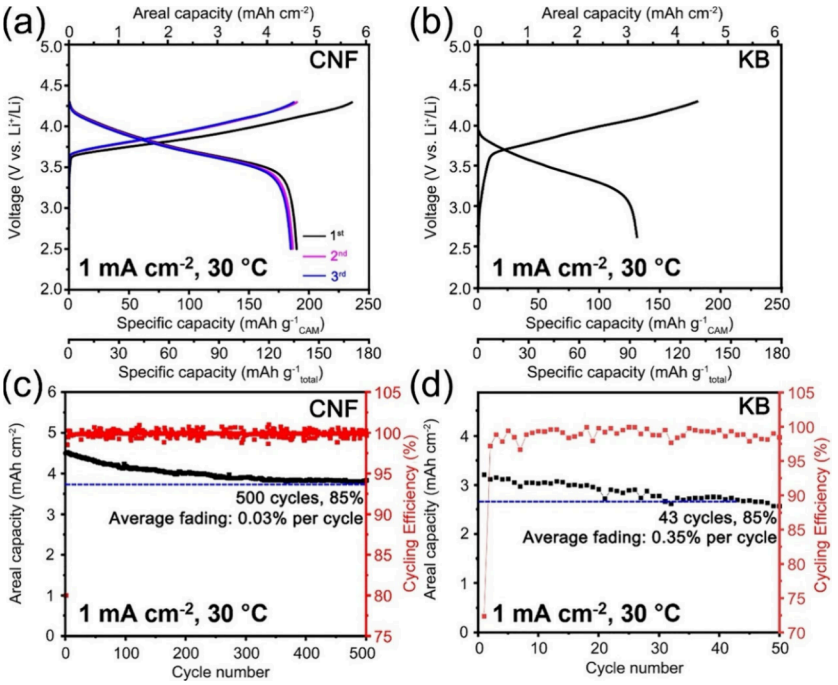

Figure 1. Electrochemical performance of the CNF- and KB-based solid-state cathodes with the same volumetric ratios of CAM: SE: carbon of 49:42:5 at 1 mA cm^{-2}, 2 MPa stack pressure, and 30 °C. (a, b) The load curves of the CNF- and KB-based solid-state cathodes over the first few cycles. The specific capacity is calculated based on the mass of the cathode active material or the total mass of the solid-state cathode. (c, d) The areal capacity and cycling efficiency of the CNF- and KB-based solid-state cathodes.

Figure 1 compares the load curves, capacity retention, and cycling efficiency of SSCs composed of CAMs, Li_6PS_5Cl and CNFs or KB. The diffraction patterns of the components are shown in Figure S1 and the morphologies are shown in Figure S2, with average particle sizes of several hundred nanometers for Li_6PS_5Cl, ~20 nm for KB, and 1−5 μm for the single-crystal NMC particles. The CNF is graphitized carbon with a diameter of 50−200 nm and a length of 20−200 μm. The CAM loading is ~ 25 mg cm^{-2} to ensure a high areal capacity and the cathode has a total thickness of ~110 μm, as confirmed by the cross-sectional plasma focused ion beam scanning electron microscopy (PFIB-SEM) image in Figure S3. The corresponding morphology and microstructure of the SSCs with CNFs and KB are further revealed via PFIB-SEM 3D reconstruction and surface SEM analyses (Figure S4 and Figure S5). The same volumetric ratios of CAM: SE: carbon of 49:42:5 were used for CNFs and KB (Figure S4). The volumetric ratios were shown previously to give the highest capacity when cycled at 30 °C, 1 mA cm^{-2} rate and low stack pressures.[7,8,11−13] A three-electrode cell with a lithium reference electrode measuring the SSC potential was used. A zero strain (no volume change) $Li_4Ti_5O_{12}$ (LTO) based composite electrode, as shown in the SEM image (Figure S5), was used as the anode in this work to enable investigation of the SSC at higher current densities without any limiting effects of a Li metal anode such as the formation of lithium dendrites. The stack pressure was 2 MPa. On constant current cycling at 1 mA cm^{-2}, the CNF-based SSC delivers an areal capacity of ~4.6 mAh cm^{-2} at 30 °C (Figure 1a and Figure S6) and ~5 mAh cm^{-2} at 60 °C (Figure S7), between 2.5 and 4.3 V, corresponding to CAM utilization of 182 mAh g^{-1} and 197 mAh g^{-1}, respectively. The cycling efficiency of the first cycle is 80% and 84%, respectively, quickly reaching and remaining above 99.5% on continuous cycling (Figure 1c and Figure S7). The relatively low first-cycle Coulombic efficiency (CE) arises from the initial interfacial side reactions at the triple-phase boundaries (TPBs) and partial contact loss between the components. As cycling proceeds, both effects are mitigated: decomposition products form a passivating layer and contact loss reaches equilibrium, leading to the rapid increase in CE. Overall, despite the use of uncoated CAMs, it exhibits a capacity retention of 85% after 500 cycles with a 0.03% capacity loss per cycle, which is ~12 times lower than KB-based SSCs (0.35% capacity loss per cycle, Figure 1b,d). Besides regulating the electronic pathways at the triple phase boundary, the improved performance at 2 MPa external stack pressure is also attributed to the zero-strain anode materials and single-crystal CAMs in this work.[7,10,11,36−46]

In this work, we used LTO to avoid complications related to dendrite formation and focus on the cathode−electrolyte interfacial processes. Importantly, changing the anode does not alter the fundamental electrochemical evolution of the composite cathode. Therefore, the TPB regulation demonstrated here is expected to be applicable to lithium metal solid-state batteries. If the problems facing the realization of a Li metal anode were solved, as shown in Figure S8, a solid-state cell incorporating this cathode would deliver an energy density of 1115 Wh L^{-1} and 1210 Wh L^{-1} with a 20 μm thick Li anode and Li_6PS_5Cl separator (Table S1), at 30 and 60 °C, respectively, where it is compared with a LIB of today.[47−51] Our calculation takes into account only the electrochemical cell components and not components, such as current collectors. The capacity retention and cycling efficiency for the CNF-based SSCs at 30 °C are comparable to those with coated CAM particles, but without of course the complexity of coatings.[8,12,20−24] They are also starkly better than that with KB in the absence of coatings as Li_6PS_5Cl oxidizes above 2.1 V.[14−19] From a manufacturing perspective, KB disperses

https://doi.org/10.1021/acsenergylett.5c02607
ACS Energy Lett. 2026, 11, 1623−1630

readily and is widely used, but its very high surface area increases the demand on binder and solvent as well as slurry viscosity, which can lower tap/areal density and complicate calendaring. In contrast, CNFs can achieve high electronic percolation at lower loadings and retain fast conductive pathways after calendaring, but their fibrous morphology requires more careful dispersion (e.g., higher shear or longer mixing) to prevent agglomeration or anisotropy. These trade-offs suggest that CNFs enable reduced total carbon content while maintaining high conductivity, whereas KB offers simpler mixing at the expense of higher carbon/binder fractions.

The measured electronic conductivity of CNF-based SSCs is higher than that of SSCs containing KB (Figure S9). The improved electronic conduction of CNF-based SSCs arises from both the intrinsically higher electronic conductivity of CNFs ($\sim 10^2-10^3$ S cm^{-1} of CNFs vs $\sim 10-10^2$ S cm^{-1} of KB) and their fibrous morphology enabling long-range electronic transport.[33,52,53] Moreover, the lower specific surface area ($\sim$24 m^2 g^{-1}, Table S2) of CNFs results in fewer TPBs and hence fewer side reactions. In contrast, the nanoparticulate morphology and high surface area ($\sim$1010 m^2 g^{-1}) of KB lead to short-range electronic pathways and a significantly higher density of TPBs, thereby promoting interfacial decomposition. These results demonstrate that CNFs enable efficient electronic percolation while minimizing undesirable side reactions, highlighting their dual role in optimizing electronic pathways and stabilizing TPBs.[16,29−33] As for the surface chemistry, Kundu et al.[54] and Kim et al.[55] have reported that the oxygen-containing functional groups can affect decomposition reactions at the TPBs. As a result, all of the carbon additives here were treated under Ar/H_2 at 500 °C and further dried at 300 °C under vacuum for 24h. The Fourier-transform infrared (FTIR) spectra (Figure S10) indicate no obvious difference among the four dried carbon additives including CNFs, KB, Super P (SP) and carbon nanotubes (CNTs).

Figure 2 shows results for SSCs composed of Li_6PS_5Cl, MnO_2 and KB or CNFs, respectively. The electronic

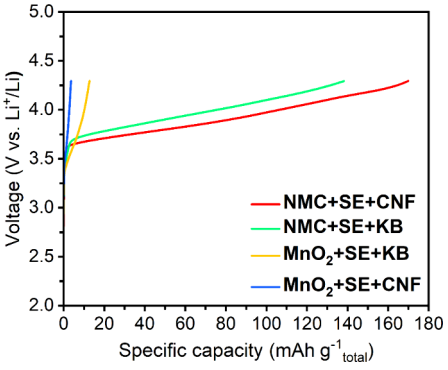

Figure 2. Comparison between solid-state cathodes with KB and CNFs on CAMs and MnO_2, respectively. The load curves of the NMC+SE+CNF, NMC+SE+KB, MnO_2+SE+KB, and MnO_2+SE +CNF cathodes at 1 mA cm^{-2}, 2 MPa stack pressure and 30 °C. The specific capacity is calculated based on the total mass of the solid-state cathode.

conductivities of high-nickel single crystal $LiNi_xMn_zCo_yO_2$ ($x + y + z = 1$)[56−59] and MnO_2[60−62] are broadly similar at $\sim 10^{-3}-10^{-5}$ and $\sim 10^{-4}-10^{-6}$ S cm^{-1}, respectively, and our measurement confirm that SSCs with NMC or MnO_2 have comparable electronic conductivities (Figure S11). Thus, replacing the active NMC with electronically inert MnO_2 does not compromise the electronic conductivity. The component ratios are identical to NMC-based SSCs (volumetric ratios 49:42:5), therefore the effect of the different carbons can be seen. The higher specific surface area of KB results in greater SE oxidation. For MnO_2-based SSCs, this is the only source of capacity. In contrast, with NMC present, there is deintercalation and now the greater direct oxidation of SE by KB compared with CNFs results in more decomposition products that increase the voltage polarization, reaching the voltage cutoff earlier (after the passage of less capacity).[16,30] In addition to CNFs and KB, we further studied the influence of conductive additives, SP ($\sim$62 m^2 g^{-1}) and CNTs ($\sim$280−350 m^2 g^{-1}) by comparing the first charge profiles of solid-state cathodes (SSCs) with NMC or MnO_2 (Figure S12).[35] SP, as a carbon black with a relatively low specific surface area (though higher than that of CNFs), provides efficient electronic conduction but introduces more TPBs, thereby promoting greater SE decomposition than CNFs. CNTs, with their one-dimensional morphology and moderately high specific surface area (lower than KB), enable the formation of extended conductive networks with more TPBs. Consequently, CNT-based SSCs exhibit more SE decomposition than SP-based SSCs but less than KB-based SSCs.

To investigate further the differences between SSCs with CNFs and KB, X-ray photoelectron spectra (XPS) were collected for each as a function of the state of charge (sulfur in Figure 3 and phosphorus in Figure S13). Considering Figure 3, the decomposition products are in accord with those observed previously for cells with carbon black.[16,20,63,64] The pristine cells show the characteristic PS_4^{3-} and S^{2-} peaks of Li_6PS_5Cl (see XPS for SE alone in Figure S14), with evidence of minor decomposition shown by the presence of a small amount of polysulfides and marginally more decomposition in the case of KB. Differences between the SSCs with CNFs and KB are seen on charging. In both cases, the quantities of decomposition products increase with state of charge. At a higher state of charge, elemental sulfur ($-S^0-$) appears. However, the extent of decomposition is significantly greater in the case of KB than CNFs and the onset of decomposition to elemental sulfur occurs at a lower voltage, 3.8 V, in the case of KB compared with 4.3 V for CNFs. The corresponding compositional analysis is shown in the bar chart between the two sets of XPS data for CNFs and KB, respectively. Phosphorus XPS data in Figure S13 show very similar trends. They indicate the appearance of PO_x at 4.3 V for CNFs and 4 V for KB, and with more PO_x in the case of KB. This finding reinforces the sulfur XPS results and is also consistent with the time-of-flight secondary ion mass spectrometry (TOF-SIMS) data (Figure S15). These trends were further confirmed by collecting impedance data on cells with CNFs and KB, respectively (Figure S16). In the case of KB, a semicircle grows on cycling, which is consistent with a growing interphase at the triple phase boundary and is in accord with the SE decomposition. The semicircles significantly decrease when CNFs are used in the SSC, consistent with a significantly smaller amount of decomposition.

To explore how the CAM and carbon affect the decomposition individually in a practical SSC, we collected the XPS data shown in Figure 4 were collected. Figure 4a shows the results for CAMs and SEs alone without carbon charged to 4.3 V, whereas Figure 4b,c shows what happens when electrodes containing 3 wt % CNFs and KB respectively

https://doi.org/10.1021/acsenergylett.5c02607
ACS Energy Lett. 2026, 11, 1623−1630

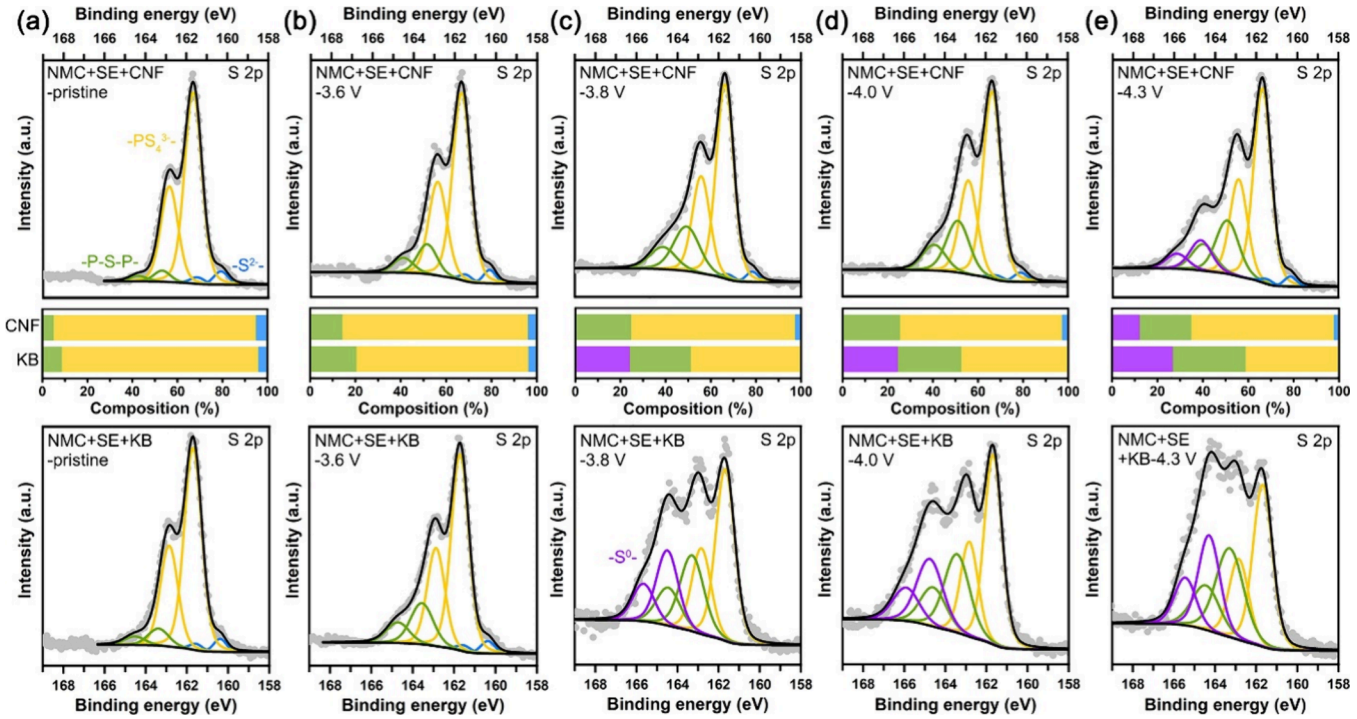

Figure 3. XPS analysis showing the different SE decomposition behaviors in the solid-state cathodes at different stages. S 2p XPS data and compositional analysis of the fitting results for the NMC+SE+CNF and NMC+SE+KB solid-state cathodes at the (a) pristine, (b) 3.6 V, (c) 3.8 V, (d) 4.0 V, and (e) 4.3 V charged states.

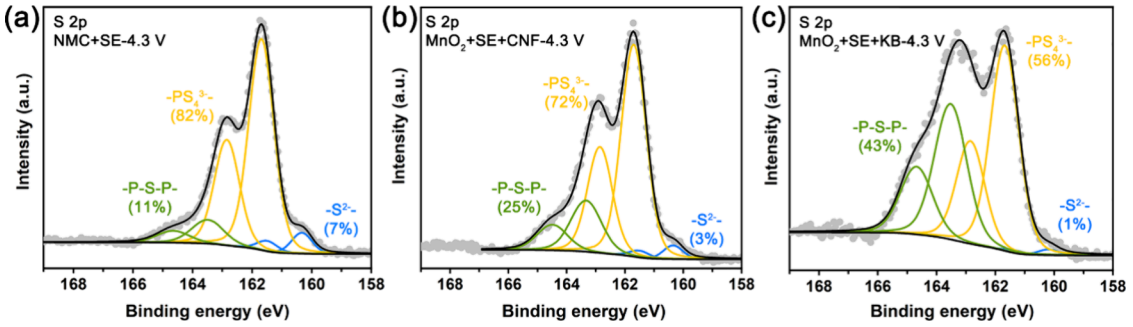

Figure 4. XPS analysis showing the effects of individual CAM or carbon on SE decomposition. S 2p XPS data of the (a) NMC+SE, (b) MnO_2+SE +CNF, and (c) MnO_2+SE+KB solid-state cathodes at the 4.3 V charged state.

are charged to the same 4.3 V but with MnO_2 instead of CAM. In all cases, decomposition only to polysulfides is observed and more predominantly for KB than CNFs in the electrodes with high CAM loading and ratio at practical cycling conditions. Crucially none of the results show decomposition to elemental $-S^0-$. Elemental $-S^0-$ occurs only when carbon and CAMs are present together in a practical SSC. It should be noted that the interfacial side reactions are regulated by both the thermodynamics and dynamics. Therefore, the composition of final interfacial byproducts could be affected by many factors such as the CAM specific surface area, carbon specific surface area, CAM ratio, carbon ratio, SSC loading, cycling current density and cycling temperature, which explains the difference of final interfacial byproducts between our findings and previous results.[65,66] However, what is clear is that the simultaneous presence of CAMs and carbon in the SSC induces more severe oxidative decomposition of the SE (*e.g.*, form elemental $-S^0-$ in our case, Figure 3 and Figure 4), pointing to the importance of where the SE, CAM and carbon meet locally. In the case of KB, the nanometer-sized carbon particles appear at numerous locations where SSEs and CAMs meet, compared with CNFs. Reaction requires the transfer of ions/electrons across the interface, and the decomposition products accumulate across this new interphase layer. The presence of numerous carbon nanoparticles at the interface could facilitate electron transfer that in turn would increase the degree of decomposition as shown in Figure 5.

It is interesting to compare the rate capability of the SSC with CNFs with the SSC in a LIB based on the liquid electrolyte (Figure 6). The two cathodes have the same volume of electrolyte except that in one case the electrolyte is Li_6PS_5Cl and in the other LP30 (1 M $LiPF_6$ in ethylene carbonate: dimethyl carbonate [1:1 v/v]). At low to intermediate rates, the capacity of the cathode is higher with the liquid electrolyte (Figure 6a), indicating that the ion transport through the composite electrode to the CAM particles is more effective due to the higher conductivity of the liquid electrolyte. However, as the rate increases, this difference decreases until at a current density of 8 mA cm^{-2}, the rate capability of the SSC exceeds that of the cathode with

https://doi.org/10.1021/acsenergylett.5c02607
ACS Energy Lett. 2026, 11, 1623−1630

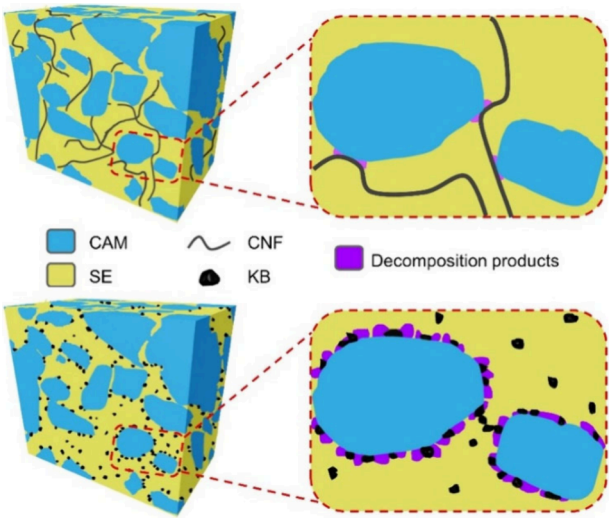

Figure 5. Schematics of the SSCs with CNFs and KB.

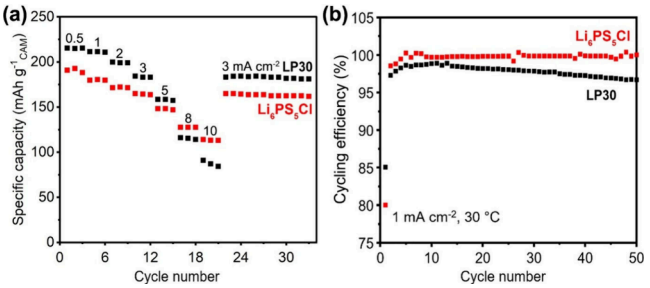

Figure 6. (a) Rate and (b) cycling efficiency comparison between cathodes with Li_6PS_5Cl and LP30 at 1 mA cm^{-2}, 2 MPa stack pressure, and between 2.5 and 4.3 V at 30 °C.

the liquid electrolyte. At high rates, cells with a liquid electrolyte can suffer from concentration polarization, where on discharge, there is depletion of salt concentration near the CAM particles, limiting the rate capability.[67] In contrast, ceramic electrolytes exhibit a transport number of 1 for the Li^+ and there is no possibility of concentration polarization.[68] The cycling efficiencies for the solid- and liquid-electrolyte-based cathodes at 1 mA cm^{-2} and 30 °C are shown in Figure 6b. In both cases, in the first cycle, the efficiencies are around 80%. The efficiencies then rise, however in the case of the SSC they remain above 99.5% whereas for LP30 the efficiency decreases continuously. These data are consistent with the continuous degradation of liquid electrolytes and the evolution of the cathode electrolyte interface layer, whereas the degradation of the SE in the SSC with a low specific surface area carbon slows significantly.[68] Increasing the electrode thickness will cause a proportional increase in charge (electrons and ions) transport distance, tortuosity and fracture and delamination, all of which will result in more Li loss and thus lower Coulombic efficiency compared to the thin electrodes (≤5 mg cm^{-2}) that were widely used in previously reports with LP30.[2,69−75] Furthermore, without the electrolyte additives such as vinylene carbonate (VC), fluoroethylene carbonate (FEC), the cycle efficiency could be further decreased as the self-passivating cathode electrolyte interphase (CEI) cannot be formed in the pristine LP30 electrolyte.[7,76,77] As a result, the low cycle efficiency with the pristine LP30 electrolyte is reasonable because we used an ∼110 μm thick electrode (∼25 mg cm^{-2}) in this work.

Although the use of CNFs as the electronic additive in the SSC suppresses the decomposition of Li_6PS_5Cl largely to the first few cycles, the decomposition does restrict the performance.[78] Raising the temperature of the cell with Li_6PS_5Cl to 80 °C results in a CAM utilization of 210 mAh g^{-1} even at a high current density of 3 mA cm^{-2} (Figure S17a), comparable to the cathode with a liquid electrolyte at 30 °C, indicating that at this temperature, mass transport through SEs and the interphase layer is no longer limiting. The cell can cycle at a much higher rate of 10 mA cm^{-2} (2 C) with utilization of the CAM at 185 mAh g^{-1} at the first cycle and 145 mAh g^{-1} after 500 cycles (Figure S17b).

The effect of double and triple phase boundaries on the SE decomposition is decoupled in the practical thick uncoated solid-state cathodes with a high CAM ratio (i.e., 75%) at practical cycling conditions. More severe oxidative decomposition of SEs only occurs when all three of the cathode active material, carbon, and the SE present simultaneously in the solid-state cathode, highlighting the importance of the triple phase boundary in decomposition and fading. The carbon nanoparticle with high specific surface area enables efficient electron transfer at the interface, increasing decomposition compared with carbon nanofibers, resulting in a lower capacity and faster fading. By regulating the electronic pathways at the triple phase boundary like using low specific surface area carbon nanofibers in solid-state cathodes, the decomposition reactions can be suppressed significantly, enabling an areal capacity of 4.6 mAh cm^{-2} ($LiNi_{0.83}Mn_{0.06}Co_{0.11}O_2$ utilization of 182 mAh g^{-1}) and ∼85% capacity retention after 500 cycles at 30 °C, 1 mA cm^{-2}, and 2 MPa between 2.5 and 4.3 V. Even without any coatings, higher $LiNi_{0.83}Mn_{0.06}Co_{0.11}O_2$ utilization and good cycling stability can be achieved via elevating the temperature. While the use of low surface area carbon nanofibers is likely beneficial generally in SSCs with other cathode active materials, such different active materials, even when combined with the same sulfide solid electrolyte used here, will result in different decomposition products and pathways.

■ ASSOCIATED CONTENT

Supporting Information

The Supporting Information is available free of charge at https://pubs.acs.org/doi/10.1021/acsenergylett.5c02607.

Experimental methods, additional PXRD, SEM, FTIR and BET results for materials, FIB-SEM images, electronic conductivity, XPS and TOF-SIMS analysis of composite cathode, dQ/dV curve, EIS, load curves and cycling performance of all-solid-state batteries or liquid batteries (PDF)

■ AUTHOR INFORMATION

Corresponding Authors

Xiangwen Gao − *Future Battery Research Centre, Global Institute of Future Technology, Shanghai Jiao Tong University, Shanghai 200240, China;* orcid.org/0000-0002-3271-912X; Email: xiangwen.gao@sjtu.edu.cn

Peter G. Bruce − *Department of Materials, University of Oxford, Oxford OX1 3PH, United Kingdom; Department of Chemistry, University of Oxford, Oxford OX1 3QZ, United*

https://doi.org/10.1021/acsenergylett.5c02607
ACS Energy Lett. 2026, 11, 1623−1630

Kingdom; orcid.org/0000-0001-6748-3084;
Email: peter.bruce@materials.ox.ac.uk

Authors

Longlong Wang − *Future Battery Research Centre, Global Institute of Future Technology, Shanghai Jiao Tong University, Shanghai 200240, China; Department of Materials, University of Oxford, Oxford OX1 3PH, United Kingdom;* orcid.org/0000-0003-0873-7405

Bingkun Hu − *Department of Materials, University of Oxford, Oxford OX1 3PH, United Kingdom;* orcid.org/0009-0008-8681-7850

Christopher Doerrer − *Department of Materials, University of Oxford, Oxford OX1 3PH, United Kingdom;* orcid.org/0000-0003-0166-6333

Shengming Zhang − *Department of Materials, University of Oxford, Oxford OX1 3PH, United Kingdom*

Lechen Yang − *Department of Materials, University of Oxford, Oxford OX1 3PH, United Kingdom;* orcid.org/0000-0002-4874-9745

Liquan Pi − *Department of Materials, University of Oxford, Oxford OX1 3PH, United Kingdom*

Max Jenkins − *Department of Materials, University of Oxford, Oxford OX1 3PH, United Kingdom*

Boyang Liu − *Department of Materials, University of Oxford, Oxford OX1 3PH, United Kingdom*

Shengda D. Pu − *Department of Materials, University of Oxford, Oxford OX1 3PH, United Kingdom*

Yi Yuan − *Department of Materials, University of Oxford, Oxford OX1 3PH, United Kingdom*

Hui Gao − *Department of Materials, University of Oxford, Oxford OX1 3PH, United Kingdom*

Alex W. Robertson − *Department of Materials, University of Oxford, Oxford OX1 3PH, United Kingdom; Department of Physics, University of Warwick, Coventry CV4 7AL, United Kingdom;* orcid.org/0000-0002-9521-6482

Patrick S. Grant − *Department of Materials, University of Oxford, Oxford OX1 3PH, United Kingdom;* orcid.org/0000-0002-7942-7837

Complete contact information is available at:
https://pubs.acs.org/10.1021/acsenergylett.5c02607

Author Contributions

#L.W., B.H., and C.D contributed equally to this work. L.W., B.H., C.D. and X.G. conceived and designed experiments. B.L., B.H. and L.Y. performed the FIB-SEM measurements. B.H. and S.Z. performed the impedance analysis. L.W., C.D. and X.G. performed the electrochemistry of solid state cells, L.W., L.P. and H.G. performed the electrochemistry of liquid electrolyte cells. L.W., Y.Y., S.D.P. and A.W.R. performed the XPS measurements and analyzed the data. M.J. performed the BET measurements. L.W. and B.H. performed the TOF-SIMS and FTIR measurements and analyzed the data. X.G., L.W., C.D., P.S.G. and P.G.B. interpreted the data. L.W., X.G. and P.G.B. wrote the paper with contributions from all authors.

Notes

The authors declare no competing financial interest.

■ ACKNOWLEDGMENTS

P.G.B. is indebted to the Faraday Institution SOLBAT (FIRG007, FIRG008, FIRG026 and FIRG056), as well as the Engineering and Physical Sciences Research Council, Enabling Next Generation Lithium Batteries (EP/M009521/1), the University of Oxford experimental equipment upgrade (EP/M02833X/1), and the Henry Royce Institute for Advanced Materials (EP/R0066X/1, EP/S019367/1, and EP/R010145/1) for financial support. X.G. acknowledges financial support from the National Natural Science Foundation of China (22309110).

■ REFERENCES

(1) Hu, X.; Zhang, Z. J.; Zhang, X.; Wang, Y.; Yang, X.; Wang, X.; Fayena-Greenstein, M.; Yehezkel, H. A.; Langford, S.; Zhou, D.; Li, B. H.; Wang, G. X.; Aurbach, D. External-pressure-electrochemistry coupling in solid-state lithium metal batteries. *Nat. Rev. Mater.* **2024**, *9* (5), 305−320.

(2) Lee, D.; Lee, H.; Song, T.; Paik, U. Toward high rate performance solid-state batteries. *Adv. Energy Mater.* **2022**, *12* (27), No. 2200948.

(3) Sandoval, S. E.; Haslam, C. G.; Vishnugopi, B. S.; Liao, D. W.; Yoon, J. S.; Park, S. H.; Wang, Y.; Mitlin, D.; Hatzell, K. B.; Siegel, D. J.; Mukherjee, P. P.; Dasgupta, N. P.; Sakamoto, J.; McDowell, M. T. Electro-chemo-mechanics of anode-free solid-state batteries. *Nat. Mater.* **2025**, *24* (5), 673−681.

(4) Janek, J.; Zeier, W. G. Challenges in speeding up solid-state battery development. *Nat. Energy* **2023**, *8* (3), 230−240.

(5) Bonnick, P.; Muldoon, J. The quest for the holy grail of solid-state lithium batteries. *Energy Environ. Sci.* **2022**, *15* (5), 1840−1860.

(6) Minnmann, P.; Strauss, F.; Bielefeld, A.; Ruess, R.; Adelhelm, P.; Burkhardt, S.; Dreyer, S. L.; Trevisanello, E.; Ehrenberg, H.; Brezesinski, T.; Richter, F. H.; Janek, J. Designing cathodes and cathode active materials for solid-state batteries. *Adv. Energy Mater.* **2022**, *12* (35), No. 2201425.

(7) Gao, X. W.; Liu, B. Y.; Hu, B. K.; Ning, Z. Y.; Jolly, D. S.; Zhang, S. M.; Perera, J.; Bu, J. F.; Liu, J. L.; Doerrer, C.; Darnbrough, E.; Armstrong, D.; Grant, P. S.; Bruce, P. G. Solid-state lithium battery cathodes operating at low pressures. *Joule* **2022**, *6* (3), 636−646.

(8) Lee, Y.-G.; Fujiki, S.; Jung, C.; Suzuki, N.; Yashiro, N.; Omoda, R.; Ko, D.-S.; Shiratsuchi, T.; Sugimoto, T.; Ryu, S.; Ku, J. H.; Watanabe, T.; Park, Y.; Aihara, Y.; Im, D.; Han, I. T. High-energy long-cycling all-solid-state lithium metal batteries enabled by silver−carbon composite anodes. *Nat. Energy* **2020**, *5* (4), 299−308.

(9) Liu, B. Y.; Pu, S. D.; Doerrer, C.; Spencer Jolly, D.; House, R. A.; Melvin, D. L. R.; Adamson, P.; Grant, P. S.; Gao, X. W.; Bruce, P. G. The effect of volume change and stack pressure on solid-state battery cathodes. *Susmat* **2023**, *3* (5), 721−728.

(10) Zhang, J.; Fu, J.; Lu, P.; Hu, G.; Xia, S.; Zhang, S.; Wang, Z.; Zhou, Z.; Yan, W.; Xia, W.; Wang, C.; Sun, X. Challenges and strategies of low-pressure all-solid-state batteries. *Adv. Mater.* **2025**, *37* (6), No. e2413499.

(11) Doerrer, C.; Capone, I.; Narayanan, S.; Liu, J.; Grovenor, C. R. M.; Pasta, M.; Grant, P. S. High energy density single-crystal NMC/Li_6PS_5Cl cathodes for all-solid-state lithium-metal batteries. *ACS Appl. Mater. Interfaces* **2021**, *13* (31), 37809−37815.

(12) Wang, Z. Y.; Xia, J. L.; Ji, X.; Liu, Y. J.; Zhang, J. X.; He, X. Z.; Zhang, W. R.; Wan, H. L.; Wang, C. S. Lithium anode interlayer design for all-solid-state lithium-metal batteries. *Nat. Energy* **2024**, *9* (3), 251−262.

(13) Wan, H.; Wang, Z.; Zhang, W.; He, X.; Wang, C. Interface design for all-solid-state lithium batteries. *Nature* **2023**, *623* (7988), 739−744.

(14) Swamy, T.; Chen, X. W.; Chiang, Y. M. Electrochemical redox behavior of Li ion conducting sulfide solid electrolytes. *Chem. Mater.* **2019**, *31* (3), 707−713.

(15) Zhu, Y.; He, X.; Mo, Y. Origin of outstanding stability in the lithium solid electrolyte materials: insights from thermodynamic analyses based on first-principles calculations. *ACS Appl. Mater. Interfaces* **2015**, *7* (42), 23685−23693.

(16) Tan, D. H. S.; Wu, E. A.; Nguyen, H.; Chen, Z.; Marple, M. A. T.; Doux, J.-M.; Wang, X.; Yang, H.; Banerjee, A.; Meng, Y. S.

Elucidating reversible electrochemical redox of Li_6PS_5Cl solid electrolyte. *ACS Energy Lett.* **2019**, *4* (10), 2418−2427.
(17) Walther, F.; Koerver, R.; Fuchs, T.; Ohno, S.; Sann, J.; Rohnke, M.; Zeier, W. G.; Janek, J. Visualization of the interfacial decomposition of composite cathodes in argyrodite-based all-solid-state batteries using time-of-flight secondary-ion mass spectrometry. *Chem. Mater.* **2019**, *31* (10), 3745−3755.
(18) Banerjee, A.; Wang, X.; Fang, C.; Wu, E. A.; Meng, Y. S. Interfaces and interphases in all-solid-state batteries with inorganic solid electrolytes. *Chem. Rev.* **2020**, *120* (14), 6878−6933.
(19) Zhang, Q.; Cao, D.; Ma, Y.; Natan, A.; Aurora, P.; Zhu, H. Sulfide-based solid-state electrolytes: synthesis, stability, and potential for all-solid-state batteries. *Adv. Mater.* **2019**, *31* (44), No. e1901131.
(20) Ma, Y.; Teo, J. H.; Kitsche, D.; Diemant, T.; Strauss, F.; Ma, Y.; Goonetilleke, D.; Janek, J.; Bianchini, M.; Brezesinski, T. Cycling performance and limitations of $LiNiO_2$ in solid-state batteries. *ACS Energy Lett.* **2021**, *6* (9), 3020−3028.
(21) Wang, L. L.; Sun, X. W.; Ma, J.; Chen, B. B.; Li, C.; Li, J. D.; Chang, L.; Yu, X. R.; Chan, T. S.; Hu, Z. W.; Noked, M.; Cui, G. L. Bidirectionally compatible buffering layer enables highly stable and conductive interface for 4.5 V sulfide-based all-solid-state lithium batteries. *Adv. Energy Mater.* **2021**, *11* (32), No. 2100881.
(22) Wang, L.; Mukherjee, A.; Kuo, C. Y.; Chakrabarty, S.; Yemini, R.; Dameron, A. A.; DuMont, J. W.; Akella, S. H.; Saha, A.; Taragin, S.; Aviv, H.; Naveh, D.; Sharon, D.; Chan, T. S.; Lin, H. J.; Lee, J. F.; Chen, C. T.; Liu, B.; Gao, X.; Basu, S.; Hu, Z.; Aurbach, D.; Bruce, P. G.; Noked, M. High-energy all-solid-state lithium batteries enabled by Co-free $LiNiO_2$ cathodes with robust outside-in structures. *Nat. Nanotechnol.* **2024**, *19* (2), 208−218.
(23) Liu, Y.; Yu, T.; Xu, S.; Sun, Y.; Li, J.; Xu, X.; Li, H.; Zhang, M.; Tian, J.; Hou, R.; Rao, Y.; Zhou, H.; Guo, S. Constructing an oxyhalide interface for 4.8 V-tolerant high-nickel cathodes in all-solid-state lithium-ion batteries. *Angew. Chem., Int. Ed.* **2024**, *63* (33), No. e202403617.
(24) Huang, Y. Y.; Zhou, L. D.; Li, C.; Yu, Z.; Nazar, L. F. Waxing bare high-voltage cathode surfaces to enable sulfide solid-state batteries. *ACS Energy Lett.* **2023**, *8* (11), 4949−4956.
(25) Zhou, L. D.; Zuo, T. T.; Kwok, C. Y.; Kim, S. Y.; Assoud, A.; Zhang, Q.; Janek, J.; Nazar, L. F. High areal capacity, long cycle life 4 V ceramic all-solid-state Li-ion batteries enabled by chloride solid electrolytes. *Nat. Energy* **2022**, *7* (1), 83−93.
(26) Zhang, Y. Q.; Tian, Y. S.; Xiao, Y. H.; Miara, L. J.; Aihara, Y.; Tsujimura, T.; Shi, T.; Scott, M. C.; Ceder, G. Direct visualization of the interfacial degradation of cathode coatings in solid state batteries: a combined experimental and computational study. *Adv. Energy Mater.* **2020**, *10* (27), No. 1903778.
(27) Xiao, Y. H.; Miara, L. J.; Wang, Y.; Ceder, G. Computational screening of cathode coatings for solid-state batteries. *Joule* **2019**, *3* (5), 1252−1275.
(28) Wang, C.; Liang, J.; Kim, J. T.; Sun, X. Prospects of halide-based all-solid-state batteries: from material design to practical application. *Sci. Adv.* **2022**, *8* (36), No. eadc9516.
(29) Mizuno, F.; Hayashi, A.; Tadanaga, K.; Tatsumisago, M. Design of composite positive electrode in all-solid-state secondary batteries with Li_2S-P_2S_5 glass−ceramic electrolytes. *J. Power Sources* **2005**, *146* (1−2), 711−714.
(30) Zhang, W.; Leichtweiss, T.; Culver, S. P.; Koerver, R.; Das, D.; Weber, D. A.; Zeier, W. G.; Janek, J. The detrimental effects of carbon additives in $Li_{10}GeP_2S_{12}$-based solid-state batteries. *ACS Appl. Mater. Interfaces* **2017**, *9* (41), 35888−35896.
(31) Quemin, E.; Dugas, R.; Koc, T.; Hennequart, B.; Chometon, R.; Tarascon, J. M. Decoupling parasitic reactions at the positive electrode interfaces in argyrodite-based systems. *ACS Appl. Mater. Interfaces* **2022**, *14* (43), 49284−49294.
(32) Mizuno, F.; Hayashi, A.; Tadanaga, K.; Tatsumisago, M. Effects of conductive additives in composite positive electrodes on charge-discharge behaviors of all-solid-state lithium secondary batteries. *J. Electrochem. Soc.* **2005**, *152* (8), A1499−A1503.
(33) Yoon, K.; Kim, J. J.; Seong, W. M.; Lee, M. H.; Kang, K. Investigation on the interface between $Li_{10}GeP_2S_{12}$ electrolyte and carbon conductive agents in all-solid-state lithium battery. *Sci. Rep.* **2018**, *8* (1), 8066.
(34) Kim, H. S.; Park, S.; Kang, S. R.; Jung, J. Y.; Kim, K.; Yu, J. S.; Kim, D. W.; Lee, J. W.; Sun, Y. K.; Cho, W. S. Accelerated degradation of all-solid-state batteries induced through volumetric occupation of the carbon additive in the solid electrolyte domain. *Adv. Funct. Mater.* **2024**, *34* (49), No. 2409318.
(35) Randau, S.; Walther, F.; Neumann, A.; Schneider, Y.; Negi, R. S.; Mogwitz, B.; Sann, J.; Becker-Steinberger, K.; Danner, T.; Hein, S.; Latz, A.; Richter, F. H.; Janek, J. On the additive microstructure in composite cathodes and alumina-coated carbon microwires for improved all-solid-state batteries. *Chem. Mater.* **2021**, *33* (4), 1380−1393.
(36) Han, Y.; Jung, S. H.; Kwak, H.; Jun, S.; Kwak, H. H.; Lee, J. H.; Hong, S. T.; Jung, Y. S. Single- or poly-crystalline Ni-rich layered cathode, sulfide or halide solid electrolyte: which will be the winners for all-solid-state batteries? *Adv. Energy Mater.* **2021**, *11* (21), No. 2100126.
(37) Kim, S.; Cha, H. Y. Y.; Kostecki, R.; Chen, G. Y. Composite cathode design for high-energy all-solid-state lithium batteries with long cycle life. *ACS Energy Lett.* **2023**, *8* (1), 521−528.
(38) Son, J. P.; Kim, J.-S.; Lee, C.-G.; Park, J.; Kim, J. S.; Kim, S.-H.; Gault, B.; Seo, D.-H.; Jung, Y. S. Dual-function ZnO-Li_3TaO_4 surface modification of single-crystalline Ni-rich cathodes for all-solid-state batteries. *ACS Energy Lett.* **2024**, *9* (11), 5403−5412.
(39) Jangid, M. K.; Cho, T. H.; Ma, T.; Liao, D. W.; Kim, H.; Kim, Y.; Chi, M.; Dasgupta, N. P. Eliminating chemo-mechanical degradation of lithium solid-state battery cathodes during >4.5 V cycling using amorphous Nb_2O_5 coatings. *Nat. Commun.* **2024**, *15* (1), No. 10233.
(40) Doerrer, C.; Metzler, M.; Matthews, G.; Bu, J. F.; Spencer-Jolly, D.; Bruce, P. G.; Pasta, M.; Grant, P. S. Spraying Li_6PS_5Cl and silver-carbon multilayers to facilitate large-scale fabrication of all-solid-state batteries. *Device* **2024**, *2* (8), No. 100468.
(41) Zhao, W.; Zhang, Y.; Sun, N.; Liu, Q. S.; An, H. W.; Song, Y. J.; Deng, B.; Wang, J.; Yin, G. P.; Kong, F. P.; Lou, S. F.; Wang, J. J. Maintaining interfacial transports for sulfide-based all-solid-state batteries operating at low external pressure. *ACS Energy Lett.* **2023**, *8* (12), 5050−5060.
(42) Tian, R. Z.; Wang, Z. Y.; Liao, J. G.; Zhang, H. Z.; Song, D. W.; Zhu, L. Y.; Zhang, L. Q. High-voltage stability of small-size single crystal Ni-rich layered cathode for sulfide-based all-solid-state lithium battery at 4.5 V. *Adv. Energy Mater.* **2023**, *13* (26), No. 2300850.
(43) Liu, X. S.; Zheng, B. Z.; Zhao, J.; Zhao, W. M.; Liang, Z. T.; Su, Y.; Xie, C. P.; Zhou, K.; Xiang, Y. X.; Zhu, J. P.; Wang, H. C.; Zhong, G. M.; Gong, Z. L.; Huang, J. Y.; Yang, Y. Electrochemo-mechanical effects on structural integrity of Ni-rich cathodes with different microstructures in all solid-state batteries. *Adv. Energy Mater.* **2021**, *11* (8), No. 2003583.
(44) Wang, C. H.; Yu, R. Z.; Hwang, S.; Liang, J. W.; Li, X. N.; Zhao, C. T.; Sun, Y. P.; Wang, J. W.; Holmes, N.; Li, R. Y.; Huang, H.; Zhao, S. Q.; Zhang, L.; Lu, S. G.; Su, D.; Sun, X. L. Single crystal cathodes enabling high-performance all-solid-state lithium-ion batteries. *Energy Storage Mater.* **2020**, *30*, 98−103.
(45) Wang, Y.; Li, X. Fast kinetics design for solid-state battery device. *Adv. Mater.* **2024**, *36* (15), No. e2309306.
(46) Lee, C.; Kim, J. Y.; Bae, K. Y.; Kim, T.; Jung, S. J.; Son, S.; Lee, H. W. Enhancing electrochemomechanics: how stack pressure regulation affects all-solid-state batteries. *Energy Storage Mater.* **2024**, *66*, No. 103196.
(47) Lin, D.; Liu, Y.; Cui, Y. Reviving the lithium metal anode for high-energy batteries. *Nat. Nanotechnol.* **2017**, *12* (3), 194−206.
(48) Wang, Z. Y.; Zhao, C. Z.; Sun, S.; Liu, Y. K.; Wang, Z. X.; Li, S.; Zhang, R.; Yuan, H.; Huang, J. Q. Achieving high-energy and high-safety lithium metal batteries with high-voltage-stable solid electrolytes. *Matter* **2023**, *6* (4), 1096−1124.

https://doi.org/10.1021/acsenergylett.5c02607
ACS Energy Lett. 2026, 11, 1623−1630

(49) Lennartz, P.; Paren, B. A.; Herzog-Arbeitman, A.; Chen, X. C.; Johnson, J. A.; Winter, M.; Shao-Horn, Y.; Brunklaus, G. Practical considerations for enabling Lilpolymer electrolyte batteries. *Joule* **2023**, *7* (7), 1471−1495.
(50) Duffner, F.; Kronemeyer, N.; Tübke, J.; Leker, J.; Winter, M.; Schmuch, R. Post-lithium-ion battery cell production and its compatibility with lithium-ion cell production infrastructure. *Nat. Energy* **2021**, *6* (2), 123−134.
(51) Balaish, M.; Gonzalez-Rosillo, J. C.; Kim, K. J.; Zhu, Y. T.; Hood, Z. D.; Rupp, J. L. M. Processing thin but robust electrolytes for solid-state batteries. *Nat. Energy* **2021**, *6* (3), 227−239.
(52) Lu, X.; Lian, G. J.; Parker, J.; Ge, R.; Sadan, M. K.; Smith, R. M.; Cumming, D. Effect of carbon blacks on electrical conduction and conductive binder domain of next-generation lithium-ion batteries. *J. Power Sources* **2024**, *592*, No. 233916.
(53) Ardanuy, M.; Rodríguez-Perez, M. A.; Algaba, I. Electrical conductivity and mechanical properties of vapor-grown carbon nanofibers/trifunctional epoxy composites prepared by direct mixing. *Compos. Part B-Eng.* **2011**, *42* (4), 675−681.
(54) Bhadra, A.; Brunisholz, M.; Bonsu, J. O.; Kundu, D. Carbon mediated in situ cathode interface stabilization for high rate and highly stable operation of all-solid-state lithium batteries. *Adv. Energy Mater.* **2025**, *15* (14), No. 2403608.
(55) Park, S. W.; Oh, G.; Park, J. W.; Ha, Y. C.; Lee, S. M.; Yoon, S. Y.; Kim, B. G. Graphitic hollow nanocarbon as a promising conducting agent for solid-state lithium batteries. *Small* **2019**, *15* (18), No. e1900235.
(56) Heenan, T. M. M.; Wade, A.; Tan, C.; Parker, J. E.; Matras, D.; Leach, A. S.; Robinson, J. B.; Llewellyn, A.; Dimitrijevic, A.; Jervis, R.; Quinn, P. D.; Brett, D. J. L.; Shearing, P. R. Identifying the origins of microstructural defects such as cracking within Ni-rich NMC811 cathode particles for lithium-ion batteries. *Adv. Energy Mater.* **2020**, *10* (47), No. 2002655.
(57) Eshetu, G. G.; Zhang, H.; Judez, X.; Adenusi, H.; Armand, M.; Passerini, S.; Figgemeier, E. Production of high-energy Li-ion batteries comprising silicon-containing anodes and insertion-type cathodes. *Nat. Commun.* **2021**, *12* (1), 5459.
(58) Hu, J.; Wang, H.; Xiao, B.; Liu, P.; Huang, T.; Li, Y.; Ren, X.; Zhang, Q.; Liu, J.; Ouyang, X.; Sun, X. Challenges and approaches of single-crystal Ni-rich layered cathodes in lithium batteries. *Natl. Sci. Rev.* **2023**, *10* (12), No. nwad252.
(59) Manthiram, A.; Knight, J. C.; Myung, S. T.; Oh, S. M.; Sun, Y. K. Nickel-rich and lithium-rich layered oxide cathodes: progress and perspectives. *Adv. Energy Mater.* **2016**, *6* (1), No. 1501010.
(60) Lan, B.; Zheng, X.; Cheng, G.; Han, J.; Li, W.; Sun, M.; Yu, L. The art of balance: engineering of structure defects and electrical conductivity of α-MnO_2 for oxygen reduction reaction. *Electrochim. Acta* **2018**, *283*, 459−466.
(61) Tang, C.; Wang, X.; Ma, M.; Wang, Z.; Li, Y.; Li, H.; Li, B.; Zhang, Y.; Zhu, X. Optimizing the electrons/ions diffusion kinetics in δ-MnO_2 for realizing an ultra-high rate-capability supercapacitor. *Chem. Eng. J.* **2023**, *471*, No. 144784.
(62) Mao, W. F.; Ai, G.; Dai, Y. L.; Fu, Y. B.; Ma, Y.; Shi, S. W.; Soe, R.; Zhang, X. H.; Qu, D. Y.; Tang, Z. Y.; Battaglia, V. S. In-situ synthesis of MnO_2@CNT microsphere composites with enhanced electrochemical performances for lithium-ion batteries. *J. Power Sources* **2016**, *310*, 54−60.
(63) Kim, U. H.; Yu, T. Y.; Lee, J. W.; Lee, H. U.; Belharouak, I.; Yoon, C. S.; Sun, Y. K. Microstructure- and interface-modified Ni-rich cathode for high-energy-density all-solid-state lithium batteries. *ACS Energy Lett.* **2023**, *8* (1), 809−817.
(64) Ma, Y.; Teo, J. H.; Walther, F.; Ma, Y. J.; Zhang, R. Z.; Mazilkin, A.; Tang, Y. S.; Goonetilleke, D.; Janek, J.; Bianchini, M.; Brezesinski, T. Advanced nanoparticle coatings for stabilizing layered Ni-rich oxide cathodes in solid-state batteries. *Adv. Funct. Mater.* **2022**, *32* (23), No. 2111829.
(65) Ohno, S.; Rosenbach, C.; Dewald, G. F.; Janek, J.; Zeier, W. G. Linking solid electrolyte degradation to charge carrier transport in the thiophosphate-based composite cathode toward solid-state lithium-sulfur batteries. *Adv. Funct. Mater.* **2021**, *31* (18), No. 2010620.
(66) Lelotte, B.; Vaz, C. A. F.; Xu, L.; Borca, C. N.; Huthwelker, T.; Pele, V.; Jordy, C.; Gubler, L.; El Kazzi, M. Spatio-chemical deconvolution of the $LiNi_{0.6}Co_{0.2}Mn_{0.2}O_2/Li_6PS_5Cl$ interphase layer in all-solid-state batteries using combined X-ray spectroscopic methods. *ACS Appl. Mater. Interfaces* **2025**, *17* (9), 14645−14659.
(67) Liu, Y. Y.; Zhu, Y. Y.; Cui, Y. Challenges and opportunities towards fast-charging battery materials. *Nat. Energy* **2019**, *4* (7), 540−550.
(68) Weiss, M.; Ruess, R.; Kasnatscheew, J.; Levartovsky, Y.; Levy, N. R.; Minnmann, P.; Stolz, L.; Waldmann, T.; Wohlfahrt-Mehrens, M.; Aurbach, D.; Winter, M.; Ein-Eli, Y.; Janek, J. Fast charging of lithium-ion batteries: a review of materials aspects. *Adv. Energy Mater.* **2021**, *11* (33), No. 2101126.
(69) Kuang, Y. D.; Chen, C. J.; Kirsch, D.; Hu, L. B. Thick electrode batteries: principles, opportunities, and challenges. *Adv. Energy Mater.* **2019**, *9* (33), No. 1901457.
(70) Chen, Y. J.; Zhao, B.; Yang, Y.; Cao, A. Y. Toward high-areal-capacity electrodes for lithium and sodium ion batteries. *Adv. Energy Mater.* **2022**, *12* (44), No. 2201834.
(71) Yang, X.; Doyle-Davis, K.; Gao, X.; Sun, X. Recent progress and perspectives on designing high-performance thick electrodes for all-solid-state lithium batteries. *eTransportation* **2022**, *11*, No. 100152.
(72) Fu, X. W.; Zhou, Y. H.; Huang, J. Y.; Feng, L. X.; Yu, P.; Zhang, Q.; Yang, W.; Wang, Y. Rethinking the electrode multiscale microstructures: a review on structuring strategies toward battery manufacturing genome. *Adv. Energy Mater.* **2023**, *13* (32), No. 2301385.
(73) McNulty, R. C.; Hampson, E.; Cutler, L. N.; Grey, C. P.; Dose, W. M.; Johnson, L. R. Understanding the limits of Li-NMC811 half-cells. *J. Mater. Chem. A* **2023**, *11* (34), 18302−18312.
(74) Fu, K.; Li, X.; Sun, K.; Zhang, Z.; Yang, H.; Gong, L.; Qin, G.; Hu, D.; Li, T.; Tan, P. Rational design of thick electrodes in lithium-ion batteries by re-understanding the relationship between thermodynamics and kinetics. *Adv. Funct. Mater.* **2024**, *34* (51), No. 2409623.
(75) Song, A. M.; Zhang, W. J.; Ma, L.; Lai, Y. C.; Zhao, Y. H.; Zhu, J. F.; Huang, M. J.; Wang, L.; Dong, L.; Li, N.; Shen, C.; Xie, K. Y. Decoupling ion-electron transport in thick solid-state battery electrodes. *ACS Energy Lett.* **2024**, *9* (10), 5027−5036.
(76) Xu, K. Electrolytes and interphases in Li-ion batteries and beyond. *Chem. Rev.* **2014**, *114* (23), 11503−11618.
(77) Xu, K. Nonaqueous liquid electrolytes for lithium-based rechargeable batteries. *Chem. Rev.* **2004**, *104* (10), 4303−4417.
(78) Walther, F.; Randau, S.; Schneider, Y.; Sann, J.; Rohnke, M.; Richter, F. H.; Zeier, W. G.; Janek, J. Influence of carbon additives on the decomposition pathways in cathodes of lithium thiophosphate-based all-solid-state batteries. *Chem. Mater.* **2020**, *32* (14), 6123−6136.

https://doi.org/10.1021/acsenergylett.5c02607
ACS Energy Lett. 2026, 11, 1623−1630